

Thickness-dependent energetics for Pb adatoms on low-index Pb nanofilm surfaces: First-principles calculations

Wei Li,¹ Li Huang,^{1,*} Raj Ganesh S. Pala,^{2,3} Guang-Hong Lu,^{4,5} Feng Liu,⁶ James W. Evans,^{7,8} and Yong Han^{7,8,†}

¹*Department of Physics, Southern University of Science and Technology, Shenzhen, Guangdong 518055, People's Republic of China*

²*Department of Chemical Engineering, Indian Institute of Technology Kanpur, UP, 208016, India*

³*Material Science Programme, Indian Institute of Technology Kanpur, UP, 208016, India*

⁴*Department of Physics, Beihang University, Beijing 100191, China*

⁵*Beijing Key Laboratory of Advanced Nuclear Materials and Physics, Beihang University, Beijing 100191, China*

⁶*Department of Materials Science and Engineering, University of Utah, Salt Lake City, Utah 84112, USA*

⁷*Department of Physics and Astronomy, Iowa State University, Ames, Iowa 50011, USA*

⁸*Ames Laboratory—U.S. Department of Energy, Iowa State University, Ames, Iowa 50011, USA*

(Received 11 June 2017; revised manuscript received 24 September 2017; published 6 November 2017)

Adsorption, interaction, and diffusion of adatoms on surfaces control growth and relaxation of epitaxial nanostructures and nanofilms. Previous reports of key diffusion barriers for Pb diffusion on low-index Pb surfaces are limited in scope and accuracy. Thus, we apply density functional theory (DFT) to calculate the adsorption and diffusion energetics for a Pb adatom on Pb(111), Pb(100), and Pb(110) nanofilms with different thicknesses. We find that these quantities exhibit damped oscillatory variation with increasing film thickness. For Pb(111) films, energetics along the minimum energy path for Pb adatom diffusion between adjacent fcc and hcp sites varies significantly with film thickness, its form differing from other metal-on-metal(111) systems. For Pb(111) and Pb(100) nanofilms, diffusion barriers obtained for both adatom hopping and exchange mechanism differ significantly from previous DFT results. Hopping is favored over exchange for Pb(111), and the opposite applies for Pb(100). For Pb(110) nanofilms, Pb adatom hopping over an in-channel bridge is most facile, then in-channel exchange, then cross-channel exchange, with cross-channel hopping least favorable. We also assess lateral Pb adatom interactions, and characterize island nucleation during deposition on Pb(111).

DOI: [10.1103/PhysRevB.96.205409](https://doi.org/10.1103/PhysRevB.96.205409)

I. INTRODUCTION

Epitaxial growth and relaxation of Pb nanostructures and nanofilms is of continuing interest [1–32]. Diffusion of Pb adatoms on film surfaces or nanostructure facets is the key underlying process. Most interest has focused on ultrathin Pb(111) nanofilms which are the prototype for quantum films, a fundamentally important condensed matter phenomenon. Such films can exhibit robust oscillations in electronic structure with increasing film thickness [33]. The physical origin of such quantum size effects (QSEs) is associated with confinement of free electrons between the upper and lower boundaries of the film, detailed behavior reflecting a matching relationship between the metal Fermi wavelength and the interlayer spacing of film [33–37]. The oscillations in electronic structure, in turn, result in the variations in other properties, e.g., thermal stability [1,3,5,6,9–12], superconducting critical temperature [38], the perpendicular upper critical field [39], surface adhesion [40], thermal-expansion coefficient [41], work function [25], conductivity [31], etc. It can be anticipated that this intriguing variation of properties as a function of film thickness has potential applications in fabrication of nanodevices with desired functionalities.

Unusual growth and relaxation kinetics have been observed from scanning tunneling microscopy (STM) experiments for Pb(111) nanofilms on Si(111)-(7 × 7). For example, the density of Pb islands nucleated during Pb deposition on Pb(111)

films with the thickness of 4 atomic layers or monolayers (ML) at 40 K is higher by a factor of 60 from that for 5-ML Pb(111) films [19,21,24]. Experiments also show distinct growth modes, e.g., formation of single- or double-layer ring structures on 5-, 6-, and 7-ML Pb(111) islands in a higher-temperature range from 180 to 240 K [15–18]. Finally, novel post-deposition coarsening behavior is also observed in these systems [20,22]. To explain such unusual behavior, some analytic theories have been suggested, and some models have been analyzed by kinetic Monte Carlo (KMC) simulations [15,17,24]. However, there remain uncertainties in part related to the complexity of such a quantum system, but also because kinetic phenomena are very sensitive to the choice of energetic parameters. This partly motivates our analysis in this work.

Recent interest has also developed in Pb adatom diffusion on other low-index faces of Pb. This derives from use of electrochemical deposition to fabricate an atomic-scale quantum conductance switch [42], noting that Pb can be utilized as an electrode material for a multivalent-metal switch [30,32,43]. Deposition of Pb atoms from the electrolyte onto Pb electrodes leads to formation of a contact with a single atom or a two-atom chain at the narrowest part of the junction [30,43]. This process is controlled by diffusion of Pb atoms on low-index (111), (100), and (110) facets (which have the lowest surface energies) of the two electrodes. Therefore, precise determination of minimum energy paths (MEPs) and corresponding diffusion barriers on these facets is important.

In this work, we perform extensive first-principles density functional theory (DFT) calculations for adsorption and diffusion properties of a Pb adatom on low-index Pb(111), Pb(100), and Pb(110) nanofilms, as well as of other selected quantities.

*huangl@sustc.edu.cn

†yong@ameslab.gov

We use the climbing nudged-elastic-band (cNEB) method [44,45] to obtain MEPs for Pb adatom diffusion, considering the two basic types of surface diffusion mechanism: single adatom hopping on the surface, and exchange between the adatom and an adjacent surface-lattice atom [46,47]. Having the MEP, one can readily determine the corresponding diffusion barrier, the key quantity for modeling epitaxial growth of nanostructures.

In Sec. II we first describe the DFT method used in our calculations. Then, to verify the reliability of different density functionals, we determine the bulk properties of fcc Pb crystal and surface energies of three types of low-index Pb nanofilms, and compare the obtained DFT values with experimental values. Third, we present the formulation for calculating adsorption energies, diffusion barriers, and corresponding diffusion rates. Fourth, we describe the determination of lateral interactions between adatoms on Pb film surfaces. These barriers and interactions are needed for modeling film growth and relaxation. In Secs. III, IV, and V we show and discuss the DFT results for adsorption and diffusion of Pb adatoms on Pb(111), Pb(100), and Pb(110) nanofilms, respectively. In Sec. VI we discuss some consequences of our results for Pb on Pb(111) for island nucleation on this surface. Finally, in Sec. VII we provide a summary.

II. DFT METHODOLOGY AND KEY ANALYSES

Our DFT calculations are performed using the plane-wave-based Vienna *ab initio* simulation package (VASP) code [48,49]. The projector augmented-wave (PAW) method [50] is utilized for the electron-core interactions with the pseudopotentials released in 2013 by the VASP group. In previous literature [13,51,52], ultrasoft pseudopotentials [53] were employed in their DFT calculations for surface energies of Pb nanofilms. As a test, we also used ultrasoft pseudopotentials to calculate surface energies of Pb(111) nanofilms from 1 to 31 ML, and obtained almost-coincident values with those from PAW method. Thus, in this work we use the PAW method rather than computationally more expensive ultrasoft pseudopotentials [54]. In addition, our tests show that the inclusion of inner $5d^{10}$ orbitals in electronic shell (as done in previous literature [51]) is extremely expensive computationally and does not result in a significant change in surface energy. Therefore, we only take the outermost $6s^26p^2$ orbitals as valence states in our work. The energy cutoff of the plane-wave basis in our surface calculations are set to be 200 eV (versus the VASP default value of 97.973 eV), which suffices for accurately describing the energetics discussed in this work. Surfaces are represented by periodically repeated slabs. To avoid slab-slab interaction, the vacuum thickness between two adjacent slabs is always taken to be 1.6 nm. Further increasing the vacuum thickness does not significantly alter energy differences in our calculations. The converged magnitude of the forces on all relaxed atoms is always less than 0.1 eV/nm. The size of the supercell and the number of \mathbf{k} points depend on the calculated system, and will be specified in the corresponding sections below.

Predictions for surface energetics can depend on the choice of electronic exchange-correlation energy functional. Recently, Perdew *et al.* have developed a revised Perdew-Burke-

TABLE I. Lattice constant a (in nm), cohesive energy E_c (in eV/atom), bulk modulus B (in GPa), and relaxed monovacancy formation energy E_f^{1v} (in eV) of bulk fcc Pb crystal from our PBE and PBEsol calculations, compared with experimental values.

	a	E_c	B	E_f^{1v}
PBE	0.5028	2.99	40.5	0.42
PBEsol	0.4928	3.38	48.5	0.52
Experiment	0.4915 ^a	2.03 ^b	47.3 ^c	$\geq 0.53^d$ 0.50 ^e 0.58 ^f

^aExtrapolation to 0 K [56].

^bExtrapolation to 0 K [57].

^cAfter removal of finite-temperature and zero-point effects [58].

^dDilatometric and x-ray measurements [59].

^eAngular correlation measurements [60].

^fAngular correlation measurements [61].

Ernzerhof (PBE) generalized gradient approximation (GGA) that can improve equilibrium properties of densely packed solids and their surfaces [55]. The abbreviation ‘‘PBEsol’’ is used to denote this functional. Given our focus on surface properties, we primarily utilize the PBEsol functional but compare against predictions from the original PBE functional for bulk properties of fcc Pb, and also for surface energies of three types of low-index Pb films.

A. Bulk properties

We first calculate the bulk properties of fcc Pb crystal, including lattice constant a , cohesive energy E_c , bulk modulus B , and relaxed monovacancy formation energy E_f^{1v} , by using both PBE and PBEsol functionals, respectively. Table I shows that values of a , B , and E_f^{1v} from PBEsol are much closer to experiment than the values from PBE, although the E_c value from PBE is slightly better than that from PBEsol. Thus, overall PBEsol GGA is more reliable than PBE GGA for calculating the bulk properties of Pb crystal.

In the calculations for a and E_c , we use the primitive cell and a \mathbf{k} mesh of $61 \times 61 \times 61$ with an energy cutoff of 400 eV. For B , we use a cubic cell of $1 \times 1 \times 1$ (in units of a) and a \mathbf{k} mesh of $61 \times 61 \times 61$ with an energy cutoff of 200 eV. For E_f^{1v} , we use a cubic cell of $4 \times 4 \times 4$ and a \mathbf{k} mesh of $5 \times 5 \times 5$ with an energy cutoff of 200 eV.

B. Surface energies

For comparison with the film thickness dependence of adsorption and diffusion properties in following sections, we first benchmark the behavior of surface energies for three types of low-index Pb films. The surface energy γ of an unsupported film with thickness L is calculated as

$$\gamma(L) = \frac{E_L - N_L \sigma_{\text{bulk}}}{2A}, \quad (1)$$

where E_L is the total energy of the slab representing the film in a supercell, N_L is the total number of atoms in the supercell, A is the area of the bottom or top face of the supercell, and σ_{bulk} is the energy per atom in the bulk crystal. DFT calculations of surface energy versus film thickness for Pb(111), Pb(100), and

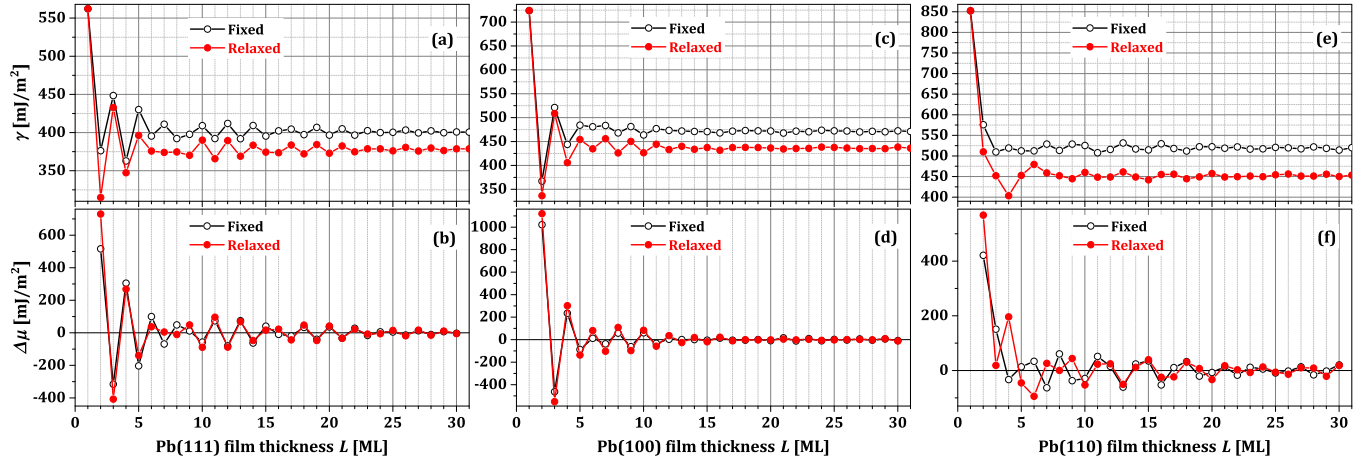


FIG. 1. Surface energies γ (upper panel) and stability indices $\Delta\mu$ (lower panel) versus Pb film thickness L from our PBEsol calculations. (a) and (b) Pb(111), (c) and (d) Pb(100), and (e) and (f) Pb(110). The curves for fixed and relaxed films are indicated by different colors and symbols.

Pb(110) using PW91 or PBE functionals have been reported previously [36,51,52,62]. Here we provide new PBEsol results which differ significantly from the PW91 or PBE results. Figures 1(a), 1(c), and 1(e) show the curves of γ as a function of film thickness from our PBEsol calculations for both fixed and relaxed Pb(111), Pb(100), and Pb(110) freestanding nanofilms, respectively. PBE results are not shown as they do not differ significantly from those obtained using old pseudopotentials available before 2013 [36].

The second-order energy difference per unit area,

$$\Delta\mu(L) = \frac{E_{L+1} + E_{L-1} - 2E_L}{A}, \quad (2)$$

measures thermodynamic stability of a nanofilm with the thickness L : for $\Delta\mu(L) < 0$, a film with L is unstable against bifurcation to thicknesses $L \pm 1$; for $\Delta\mu(L) > 0$, the film is stable [36,63]. Figures 1(b), 1(d), and 1(f) shows the stability index $\Delta\mu$ as a function of L for both fixed and relaxed Pb(111), Pb(100), and Pb(110) nanofilms, respectively. Film stability versus L and associated beat phenomenon have been reported previously [9,36].

Analysis based on a noninteracting electron-gas model (EGM) [33,36] shows that if the interlayer spacing d of a metal film is related to the half Fermi wavelength via $\lambda_F/2$, i.e.,

$$jd \approx m\lambda_F/2, \quad (3)$$

where both $j > 1$ and m are the smallest possible positive integers with no common factor, then surface energy (and other properties) as a function of film thickness will display damped oscillations with a period of jd . If $m\lambda_F/2$ is sufficiently close but not exactly equal to jd , then oscillations with a period of jd will be modulated into a beating pattern with a beat period of Λd , where

$$\Lambda = \frac{1}{|m - 2jd/\lambda_F|}. \quad (4)$$

For Pb(111) films with the experimental bulk lattice constant $a = 0.4915$ nm (corresponding interlayer spacing $d = 0.2838$ nm) and Fermi wavelength $\lambda_F = 0.3962$ nm, one can choose $j = 2$ when m is taken as the integer 3 to satisfy Eq. (3).

Thus, γ and $\Delta\mu$ will oscillate with the period of $2d = 2$ ML and with a beat period of $\Lambda d = 7.42$ ML from Eq. (4). This analysis is clearly in excellent agreement with the DFT results, as indicated by black curves with circles in Figs. 1(a) and 1(b).

For Pb(100) and Pb(110) films, oscillations in surface energy from DFT analysis [see Figs. 1(c)–1(f)] cannot be explained by EGM analysis. These oscillations have been attributed to crystalline lattice effects for the fcc metal [36]. Different arguments from band-structure analyses for bilayer oscillations in the Pb(100) surface energy [as shown in Figs. 1(c) and 1(d)] are provided by Yu *et al.* [62] and Wei *et al.* [52].

Figure 1 shows that the patterns after relaxation have subtle differences from those before relaxation. For Pb(111) films with smaller L , these differences, e.g., in amplitude, are relatively large. In particular, around the first odd-even switch point [see Fig. 1(b)], the signs of $\Delta\mu$ of $L = 7$ and 8 after relaxation become opposite to those before relaxation (the beat period is shortened by 1 ML after relaxation). The differences in $\Delta\mu$ between fixed and relaxed curves will gradually disappear with increasing L . Similar to Pb(111), the relaxation effects for Pb(100) and Pb(110) become weaker for larger L . However, relative to Pb(100), the relaxation effects for Pb(110) are overall more noticeable. A qualitative analysis of the effect of interlayer relaxation is given as Appendix A.

In Table II we compare experimental values surface energies γ_{111} , γ_{100} , and γ_{110} for bulk Pb(111), Pb(100) and Pb(110) films, respectively, with DFT values averaged over thicknesses $L = 26$ to 31. Although the L dependence from PBEsol and PBE calculations are similar, magnitudes of γ from PBEsol are much closer to experimental values.

In the DFT calculations of surface energies for Pb(111), Pb(100) and Pb(110) films, we always use a 1×1 supercell with a \mathbf{k} mesh of $51 \times 51 \times 1$. The lateral sizes m and n in any supercell $m \times n$ for calculating a surface are always in units of their corresponding surface lattice constants: $a/\sqrt{2}$ for (111) or (100); a and $a/\sqrt{2}$ for (110) along x and y directions, respectively. For details of how to extract convergent surface energies from our slab calculations, see the Supplemental Material [64].

TABLE II. Surface energies γ_{111} , γ_{100} , and γ_{110} (in units of mJ/m^2) of fixed and relaxed Pb(111), Pb(100), and Pb(110) bulk films, respectively, from our PBE and PBEsol calculations are compared with experimental values. All these bulk-film surface energies from PBE and PBEsol calculations are obtained by averaging over the film thicknesses from $L = 26$ to 31 (also see Fig. 1).

		γ_{111}	γ_{100}	γ_{110}
PBE	fixed	301	362	402
	relaxed	275	321	337
PBEsol	fixed	401	471	519
	relaxed	378	436	453
Experiment ^a		441	468	482

^aAt 323 K [65].

C. Adsorption energies, diffusion barriers, and diffusion rates

In the following sections, we will determine the variation of adsorption energies and diffusion barriers for Pb adatoms on Pb(111), Pb(100) and Pb(110) nanofilms with increasing thickness. They are key thermodynamic and kinetic quantities, respectively. As described in Sec. II, the PBEsol functional can improve predictions of most bulk properties of Pb crystal and is intended for reliable analysis of surface energies. Thus, below we mainly present PBEsol results, but sometimes also compare with PBE results.

The adsorption energy of a Pb adatom at a site of type Q on a substrate slab can be defined as

$$E_{\text{ad}}(\text{Q}) = E_{\text{Q}} - E_{\text{slab}} - E_{\text{Pb}}, \quad (5)$$

where E_{Q} is the total energy of the slab with the adatom at the site Q, E_{slab} is the total energy of slab without adatom, and E_{Pb} is the self-energy of one isolated gas-phase Pb atom. E_{Q} , E_{slab} , and E_{Pb} are directly obtained from DFT calculations. We will sometimes consider the energy difference $\Delta E(\text{Q1-Q2}) = E_{\text{ad}}(\text{Q2}) - E_{\text{ad}}(\text{Q1}) = E_{\text{Q2}} - E_{\text{Q1}}$ between two distinct types of adsorption sites Q1 and Q2. The diffusion barrier $E_{\text{d}}(\text{hop})$ for adatom hopping is defined as the energy difference (or adsorption energy difference) between the lowest-energy adsorption site and the transition state (TS), which is the highest saddle point on a MEP between

adjacent lowest-energy adsorption sites. We will also consider the diffusion barrier $E_{\text{d}}(\text{exchange})$ for two-atom exchange, which will be explicitly defined in the subsequent subsections.

For determination of diffusion rates r , either for hopping or exchange, we adopt an Arrhenius form

$$r = \nu e^{-E_{\text{d}}/(k_{\text{B}}T)}, \quad (6)$$

where ν denotes the attempt frequency, k_{B} is Boltzmann's constant, and T denotes the surface temperature. The diffusion rates provide input for modeling film growth and relaxation, as will be discussed in Sec. VI.

D. Lateral interaction energetics

Lateral interactions between Pb adatoms impact both nucleation and growth of Pb islands on a film surface during deposition, and also post-deposition coarsening. Specifically, these interactions modify rates for diffusion at islands edges and control rates for attachment-detachment processes. A simple assessment of the lateral interactions within 1 ML adsorbed on a substrate film of thickness L comes from determining the total lateral interaction per atom,

$$\Phi_{\text{tot}} = E_{1\text{ML}} - E_{\text{ad}}, \quad (7)$$

where $E_{1\text{ML}} = \Delta E_L - E_{\text{Pb}}$ contains the total adsorption plus interaction energy per atom, and $\Delta E_L = E_{L+1} - E_L$ with E_{L+1} and E_L being the total energies of 1×1 -unit-cell slabs of thicknesses $L + 1$ and L , respectively. Also, E_{ad} is the adsorption energy for an isolated adatom on a slab of thickness L at the same site as that of an atom in the adsorbed ML. It is natural to extract an effective pairwise interaction $\omega_{\text{p1,eff}}$ from Φ_{tot} . Note that each atom shares $z = 6, 4,$ and 2 effective nearest-neighbor (NN) bonds with adjacent atoms for (111), (100), and (110) surfaces, respectively. Thus, we assign

$$\omega_{\text{p1,eff}} = 2\Phi_{\text{tot}}/z. \quad (8)$$

In Fig. 2 we show $E_{1\text{ML}}$ and $\omega_{\text{p1,eff}}$ versus Pb(111), Pb(100), and Pb(110) film thickness L , using Eqs. (7) and (8). For the thicker films, our PBEsol results indicate the values of $\omega_{\text{p1,eff}}$ varying around $-0.25, -0.17,$ and -0.18 eV for Pb(111),

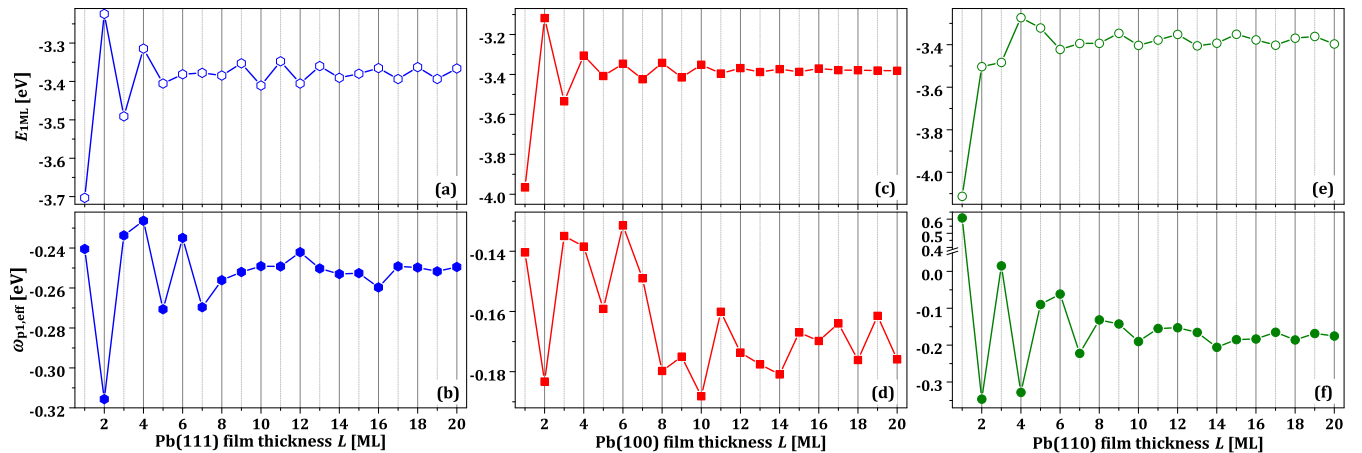


FIG. 2. Total (adsorption plus interaction) energy $E_{1\text{ML}}$ and effective pair interaction $\omega_{\text{p1,eff}}$ for 1 ML adsorbed on (a) and (b) Pb(111) fcc sites; (c) and (d) Pb(100) 4fh sites; (e) and (f) Pb(110) 4fh sites versus film thickness L from our PBEsol calculations.

Pb(100), and Pb(110) surface, respectively. For more details, see Table S1 of the Supplemental Material [64].

III. ADATOM ENERGETICS ON Pb(111)

A. Adsorption energies

Previously, Chan *et al.* [13] performed DFT calculations using ultrasoft-pseudopotential PW91 GGA for adsorption energies of a Pb adatom on Pb(111) films with the thicknesses from 3 to 9 ML. They use a unit cell of 4×4 and a \mathbf{k} mesh of $4 \times 4 \times 1$. From our tests, a larger unit cell, e.g., 5×5 at least, is necessary for convergence of adsorption energies, and thus we use the 5×5 unit cell in our PAW PBEsol calculations for adsorption energies. Also, from a series of \mathbf{k} -point convergence tests, to be more accurate, we use a \mathbf{k} mesh of $9 \times 9 \times 1$. Figure 3 shows $E_{ad}(fcc)$ and $E_{ad}(hcp)$, which are the adsorption energies of Pb adatom on hcp and fcc sites of Pb(111) film surface for film thicknesses from 1 to 20 ML, respectively. There is no distinction between fcc and hcp for $L = 1$. In the calculations of Fig. 3, we always fix the bottommost ML and relax all other atoms. Note that the values of $E_{ad}(fcc)$ and $E_{ad}(hcp)$ are calculated from Eq. (5), and have a different energy reference from the definition of Chan *et al.* [13]

Compared with Fig. 3(b) of Chan *et al.* [13], the overall shapes of curves from $L = 3$ to 9 in Fig. 3 are similar, but there are significant differences in other aspects. For example, in our results from Fig. 3, except for $L = 1$ and 7, $E_{ad}(hcp)$ is *always* lower than $E_{ad}(fcc)$ (i.e., hcp site is more favorable than fcc site for adatom adsorption), while in Chan *et al.*'s results, for 3-ML film, $E_{ad}(hcp)$ is higher than $E_{ad}(fcc)$ (i.e., the fcc site is more favorable). For comparison, we also show the adsorption energy difference $\Delta E_{ad}(hcp-fcc) = E_{ad}(fcc) - E_{ad}(hcp)$ in Fig. 3(b), which has noticeable difference in both curve shape and magnitude from Chan *et al.*'s Fig. 2(b) (where they inappropriately identify the diffusion barrier as the adsorption energy difference of a Pb adatom between fcc and hcp sites) [13]. From $L = 8$ to 9, our result shows an increase of ~ 8 meV in $\Delta E_{ad}(hcp-fcc)$, contrasting a decrease of ~ 17 meV in Chan *et al.*'s Fig. 2(b) [13]. In contrast to the γ and $\Delta\mu$ curves in Figs. 1(a) and 1(b), the E_{ad} curves in Fig. 3(a) become more irregular, and a brief analysis on this is provided in Appendix B.

B. Diffusion barriers

Previously we have used a constrained-relaxation method to estimate various diffusion barriers of a Pb adatom across or between facets of a Pb mesa using the empirical MEAM potential [20,67]. In the present work, to obtain more reliable diffusion barriers, we use the cNEB method to calculate the MEP of an adatom diffusing on the surface. Figure 4 shows the cNEB MEPs from our PBEsol calculations for a Pb adatom diffusing between NN fcc and hcp sites on 1- to 12-ML Pb(111) film surfaces, respectively. In these calculations, the fully relaxed configuration with the adatom at a hcp (fcc) site is always taken to be the first (second) cNEB endpoint and corresponds to the leftmost (rightmost) point on MEPs in Fig. 4. By symmetry, the full MEP between two NN hcp (or fcc) sites follows directly from the more restricted MEP in Fig. 4. For geometric details of fcc, hcp, and bridge sites, see the inset in Fig. 3(a).

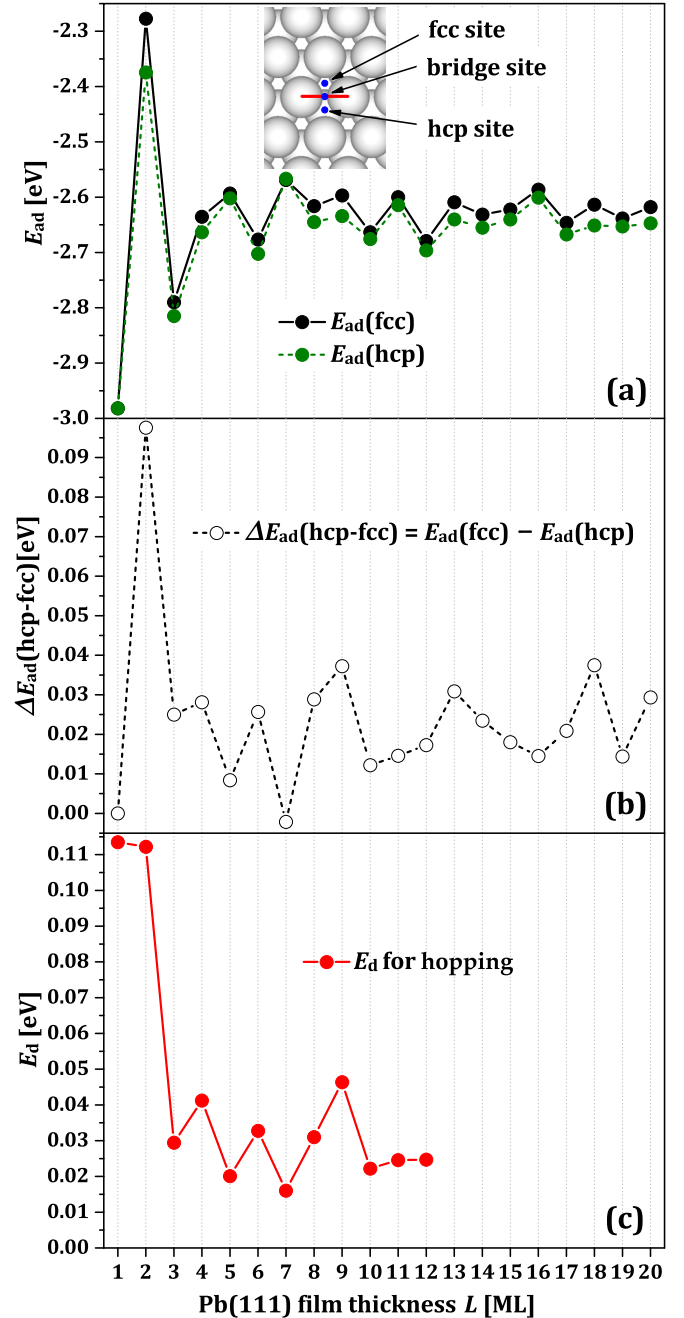


FIG. 3. (a) Adsorption energies of Pb adatom at fcc and hcp sites versus Pb(111) film thickness L from our PBEsol calculations. Inset illustrates fcc, hcp, and bridge sites of Pb(111) surface. (b) Adsorption energy difference $\Delta E_{ad}(hcp-fcc) = E_{ad}(fcc) - E_{ad}(hcp)$. (c) Diffusion barriers of Pb adatom hopping from hcp site to fcc site from our cNEB calculations. For corresponding MEPs, see Fig. 4.

From Fig. 4, for $L > 2$, the MEP curves are double-peaked ($L = 3, 5, 6, 7, 8, 10, \dots$) or nearly so ($L = 4$ and 9), in contrast to the expected single-peaked form with a maximum TS at the bridge site (e.g., that from earlier analysis with the empirical MEAM potential [67]). Consistently we checked the configuration geometry for each cNEB image, and found for $L > 2$ that the bridge site does *not* correspond to a saddle point but is often a local minimum. This does contrast behavior

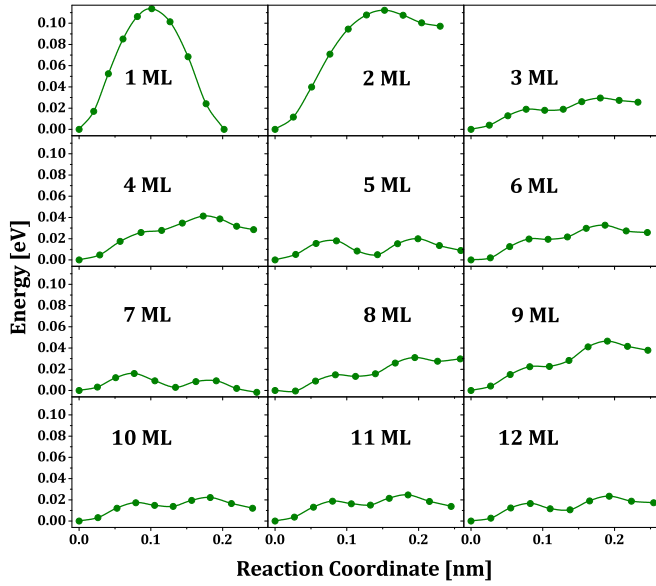


FIG. 4. MEPs of Pb adatom hopping from hcp (left endpoint) to fcc (right endpoint) sites versus Pb(111) film thickness L from our PBEsol calculations using the cNEB method. Dots represent cNEB images, and the corresponding curves are generated from a modified Bézier method [66] by fitting the energies of ten data points (dots) versus reaction coordinates. Similar statement for other MEP figures below.

for other hexagonal close-packed metal (111) surfaces. See DFT calculations by Bogicevic *et al.* [68] for Al/Al(111) and Cu/Cu(111) using a constrained-relaxation method, and by Hayat *et al.* [69] for Cu/Ag(111) using a dragging method. The unusual behavior for Pb is probably related to larger relaxation of substrate atoms (as we checked for the configuration geometries of cNEB images), i.e., Pb is liquidlike or soft, relative to Al, Cu, Ag, etc. Correspondingly, Pb has a significantly smaller

cohesive energy (2.03 eV/atom) than Al (3.39 eV/atom), Cu (3.49 eV/atom), Ag (2.95 eV/atom), etc. [57].

The diffusion barrier E_d for Pb adatom hopping from hcp site to fcc site is obtained from the difference between the energy (E_{TS}) at the highest saddle point and the energy (usually E_{hcp} at hcp site) at the most stable adsorption site. By comparing Fig. 3(c) with Figs. 3(b) and 3(a), E_d as a function of $L > 1$ is roughly in-phase with that of $\Delta E_{ad}(hcp-fcc)$, but is antiphase to E_{ad} for some L values. We also note that the oscillations in $\Delta E_{ad}(hcp-fcc)$ even up to $L = 20$ are still strong, similar to Fe/Pb(111) [70]. Because the cNEB calculations for thicker films are much more expensive, we calculate E_d only up to $L = 12$, but we believe that E_d has similar oscillations to $\Delta E_{ad}(hcp-fcc)$ for $L = 13$ to 20 (see Fig. 3). Additional information on E_d is given in Table S2 [64] including a comparison with the quite different results from Lin *et al.* [30]. In addition, one can expect that the exchange diffusion between the adatom and one (111) surface atom should be unfavorable over hopping diffusion of the adatom. Confirmation of this feature, and comparison with Lin *et al.*'s results, are provided in Appendix C.

C. Lateral interactions

Given the availability of systematic studies of the nucleation and growth of islands during Pb deposition on Pb(111), a more detailed assessment of lateral adatom interactions, which impact this process, is appropriate. Specifically, we assess the variation of these interactions with film thickness L . The values of energies from our DFT calculations are provided in Tables S2–S6 [64]. In Figs. 5(a)–5(d) we show the total adsorption plus interaction energy per adatom for a Pb pair and a trimer: $E_{p1} = (E_{dimer} - E_{slab})/2 - E_{Pb}$ and $E_{t1} = (E_{trimer} - E_{slab})/3 - E_{Pb}$, as well as pair interaction $\omega_{p1} = 2(E_{p1} - E_{ad})$ and trio interaction $\omega_{t1} = 3(E_{p1} - E_{ad} - \omega_{p1})$, where $E_{dimer(trimer)}$ is the total energy of the slab with a dimer (trimer) adsorbed at two (three) NN fcc or hcp sites (the

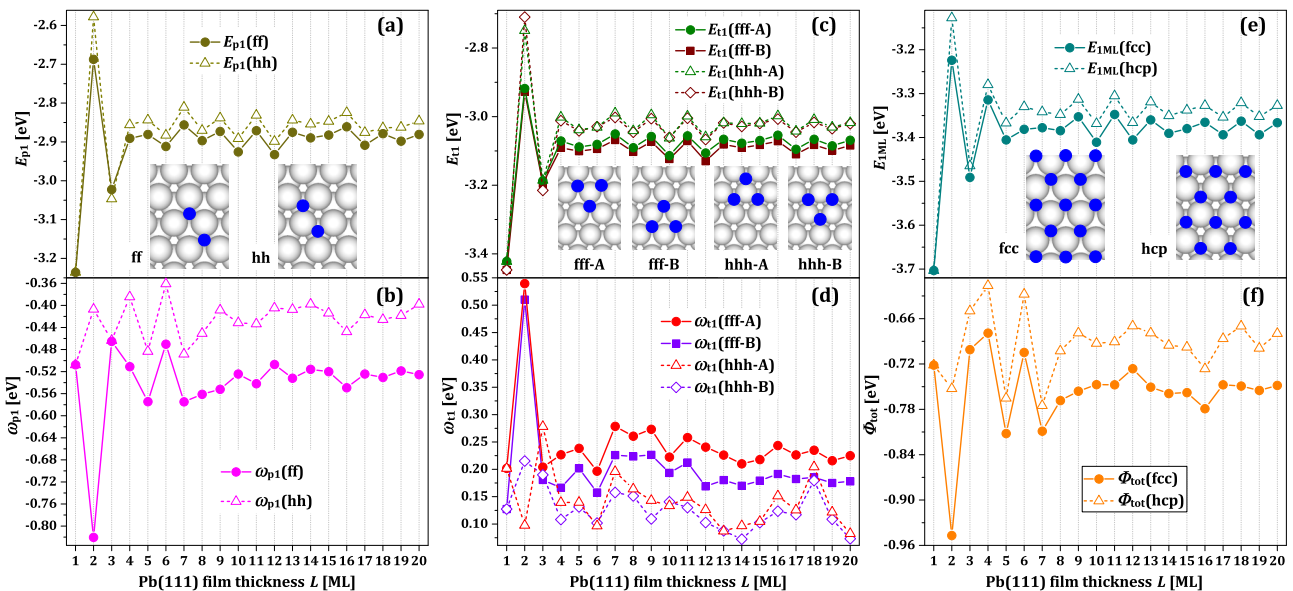


FIG. 5. Energetics for Pb (a) and (b) dimers; (c) and (d) trimers; (e) and (f) 1 ML adsorbed at fcc or hcp sites (as indicated in corresponding insets) on Pb(111) film surface versus thickness L from our PBEsol calculations. For more details, see Tables S2–S6 [64].

geometries are indicated in corresponding insets), and E_{slab} is the total energy of the clean slab. $E_{\text{dimer(trimer)}}$, E_{slab} , and E_{Pb} can be directly obtained from DFT calculations, and corresponding E_{ad} values have been shown in Fig. 3(a).

While adsorption of isolated adatoms on hcp sites is generally preferred (as discussed in Sec. III A), Pb ad-dimers generally prefer fcc sites; see Fig. 5(a). This feature is explained by the substantially stronger pair attraction between the NN Pb atoms on fcc (versus hcp) sites; see Fig. 5(b). Similarly, the trimers (of two distinct types with differing orientations A and B) also prefer fcc over hcp sites; see Fig. 5(c). More detailed analysis reveals the presence of a substantial repulsive trio interaction, which is actually stronger for the trimer on fcc sites than on hcp sites, see Fig. 5(d). However, the effect of the pair interactions dominates in determining the site preference. These observations, together with those below indicating a positive stacking fault formation energy, make it clear why fcc rather than stacking fault hcp islands nucleate and grow in this system.

We also assess the per-atom total (adsorption plus interaction) energy $E_{1\text{M}}$ for a complete layer with the atoms adsorbed on both fcc and also hcp sites. Figure 5(e) reveals that fcc stacking is always preferred [fcc energy curve here is the same as that in Fig. 2(a)]. The difference between the higher hcp and lower fcc energies corresponds to the stacking fault formation energy. From $E_{1\text{ML}}$ we can also extract the per-atom total lateral interaction energy Φ_{tot} using Eq. (7). $E_{1\text{ML}}$ and Φ_{tot} versus Pb(111) film thickness L are shown in Figs. 5(e) and 5(f), respectively. If one assumes that only NN pair interactions ω_{p1} and trio interactions ω_{t1} (A or B) are significant, then one has that $\Phi_{\text{tot}} \approx 3\omega_{\text{p1}} + \omega_{\text{t1}}(\text{A}) + \omega_{\text{t1}}(\text{B})$. However, for thicker films, e.g., for $L = 15$, $\Phi_{\text{tot}}(\text{fcc}) = -0.758$ eV versus $3\omega_{\text{p1}}(\text{ff}) + \omega_{\text{t1}}(\text{fff-A}) + \omega_{\text{t1}}(\text{fff-B}) = -1.163$ eV. This reveals the existence of additional significant lateral interactions which are overall repulsive.

IV. ADATOM ENERGETICS ON Pb(100)

A. Adsorption energies

Adsorption energies E_{ad} of a Pb adatom at 4fh and bridge sites versus Pb(100) film thickness L from our PBEsol calculations are shown in Fig. 6(a). Both $E_{\text{ad}}(4\text{fh})$ and $E_{\text{ad}}(\text{bridge})$ exhibit bilayer oscillations with the same phase, which however are opposite to the phase of γ in Fig. 1(c). This indicates that, unlike Pb(111) case, interlayer and intralayer relaxations of Pb(100) nanofilm with Pb adatoms are not strong enough to destroy the regularity of bilayer oscillations in clean Pb(100) nanofilm. In all DFT calculations for Fig. 6, we always use a 5×5 unit cell with the \mathbf{k} mesh of $9 \times 9 \times 1$, and fix the bottom 1 ML but incorporate relaxation of other atoms.

B. Diffusion barriers

For a surface system of fourfold symmetry, it is expected [46,71–74] that the hopping barrier can be simply obtained from the energy difference

$$E_{\text{d}}(\text{hop}) = \Delta E(4\text{fh-bridge}) = E_{\text{bridge}} - E_{4\text{fh}}, \quad (9)$$

where $E_{4\text{fh}}$ (E_{bridge}) is the optimized total energy of system by directly relaxing the adatom at the 4fh (bridge) site. Nonetheless, we still made a few cNEB tests for Pb on Pb(100)

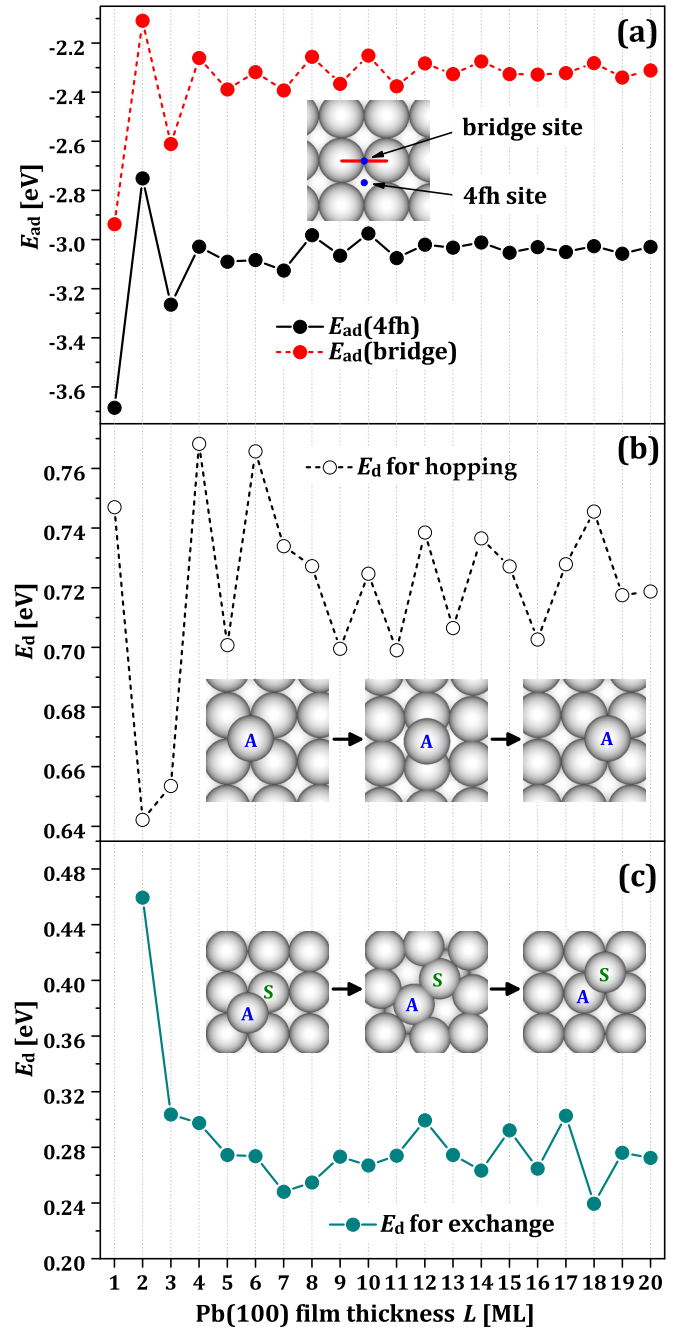


FIG. 6. (a) Adsorption energies of Pb adatom at 4fh and bridge sites versus Pb(100) film thickness L from our PBEsol calculations. Inset illustrates 4fh and bridge sites of Pb(100) surface. (b) Hopping barriers from Eq. (9). Inset indicates the hopping process for adatom A. (c) Exchange barriers from Eq. (10). Inset indicates the two-atom exchange process: the initial adatom A kicks the surface atom S out of the surface lattice and takes the place of S; simultaneously S is pushed to an adjacent 4fh site along diagonal direction and becomes a new adatom.

surface and find that the MEP energy from the cNEB method is always single-peaked, with the TS corresponding to the optimized geometry by directly relaxing Pb adatom at the bridge site. For instance, using the cNEB method for Pb adatom on a 5-ML Pb(100) film with a 3×3 unit cell and a \mathbf{k} mesh of $11 \times 11 \times 1$, we obtain a PBEsol (PBE) hopping barrier of

689 (644) meV which is consistent with results 689 (640) meV from Eq. (9). Consequently, only results from Eq. (9) are reported for Pb(100).

Similarly, the energy barrier of two-atom exchange diffusion on fcc (100) surfaces, see insets in Fig. 6(c), can also be obtained by cNEB method or by directly relaxing an appropriately built symmetric geometry. This approach was used by Feibelman for Al/Al(100), where the two-atom exchange mechanism was first proposed [46]. Then, the exchange barrier is simply obtained from

$$E_d(\text{exchange}) = E_{\text{TS}} - E_{4\text{fh}} = E_{\text{SR}} - E_{4\text{fh}}, \quad (10)$$

where E_{SR} is the optimized energy by directly relaxing the above appropriately built symmetric geometry. We describe this as the symmetric-relaxation (SR) method. As a test, using the cNEB method for Pb adatom on a 5-ML Pb(100) film with a 3×3 unit cell and a \mathbf{k} mesh of $11 \times 11 \times 1$, we obtained a PBEsol (PBE) exchange barrier of 385 (363) meV versus 386 (363) meV from the SR method using Eq. (10). In the test, we also find that the MEP curve from the cNEB method is single-peaked, and the TS just corresponds to the SR geometry. This indicates the validity of the SR method. Appendix D provides the details for how to appropriately build the initial symmetric geometry.

Diffusion barriers E_d from PBEsol calculations for hopping and exchange versus Pb(100) film thickness L are shown in Figs. 6(b) and 6(c), respectively. E_d for hopping still exhibits strong oscillations, but some odd-even switch points appear at $L = 4, 8, 15, \dots$, in contrast to the more regular bilayer oscillations in E_{ad} . E_d for exchange exhibits even more irregular oscillations, this irregularity being attributed to stronger relaxation during two-atom exchange than for adatom hopping. A key result is that the exchange barrier for each L is much smaller than the corresponding hopping barrier. For additional results, see Table S7 [64].

Besides the above “standard” two-atom exchange along the diagonal $\langle 100 \rangle$ direction, we also check the alternative exchange along the close-packed $\langle 110 \rangle$ direction as illustrated in Fig. 7. First, we perform a PBEsol cNEB calculation for Pb adatom on a 5-ML Pb(100) film, and obtain the MEP shown in Fig. 7(a). Then we also directly perform a SR calculation with an initial geometry as illustrated in left image of Fig. 7(b), and obtain the almost same energy and geometry [right image of Fig. 7(b)] as those of saddle point in Fig. 7(a). Thus, again the SR is reliable. From Fig. 7 we obtain an alternative exchange barrier of 559 meV, which is between the hopping barrier 701 meV and the standard exchange barrier 275 meV (listed in Table S7 [64]).

Previous DFT analysis by Chang *et al.* found that the standard two-atom diagonal exchange barrier of Ni adatom on Ni(100) surface depends strongly on the surface unit-cell size $n \times n$, while the barrier for hopping is almost independent of the cell size [75]. Here we also calculate the unit-cell size dependence of hopping and exchange diffusion barriers for Pb adatom on a 5-ML Pb(100) film. Figure 8 shows that unit-cell size dependence for Pb/Pb(100) is analogous to that for Ni/Ni(100) [75]. Using a 3×3 unit cell, Lin *et al.* [30] obtain a PBE hopping barrier of 640 meV, which is the same as our PBE result from the same unit-cell size; however, they obtain

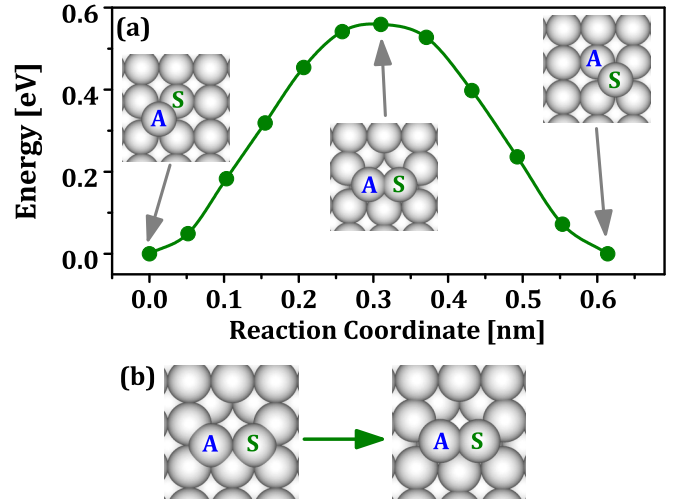


FIG. 7. (a) The cNEB MEP of two-atom exchange along the close-packed $\langle 110 \rangle$ direction on a 5-ML Pb(100) film from our PBEsol calculations. Inset shows the geometries corresponding to two endpoints and saddle point on the MEP, as indicated by arrows. (b) Left: Initial geometry used to directly obtain the TS for two-atom in-channel exchange diffusion by the SR method: initial adatom A and surface atom S are aligned along $\langle 110 \rangle$ direction at the two original 4fh sites near the vacancy, and the initial height of both is set to be $a/5$ relative to top surface atom. Right: After full relaxation of the left configuration, it is optimized to a configuration with the almost same energy and geometry as those of saddle point in (a).

a PBE exchange barrier of 470 meV, which is much larger than our result of 363 meV (see Table S8 [64]) likely because they only relax uppermost 2 ML of 5-ML Pb(100) substrate.

V. ADATOM ENERGETICS ON Pb(110)

A. Adsorption energies

Adsorption energies E_{ad} from our PBEsol calculations for a Pb adatom at 4fh sites, as well as in-channel and cross-channel

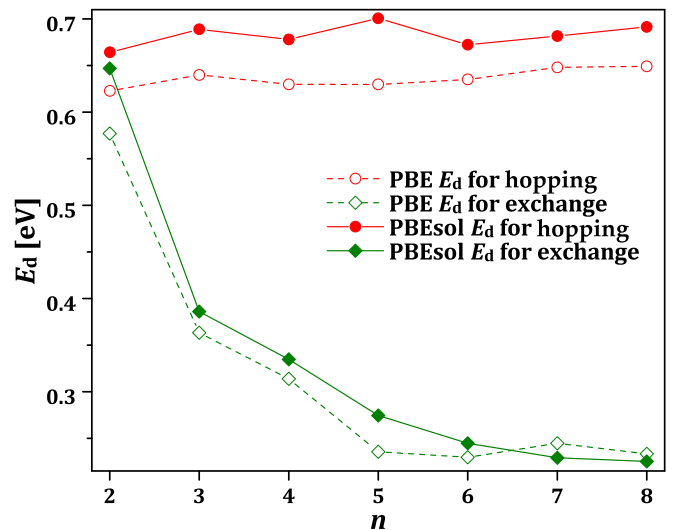


FIG. 8. Unit-cell size $n \times n$ dependence of diffusion barriers E_d for hopping and two-atom diagonal exchange from our PBEsol and PBE calculations for Pb adatom on a 5-ML Pb(100) film.

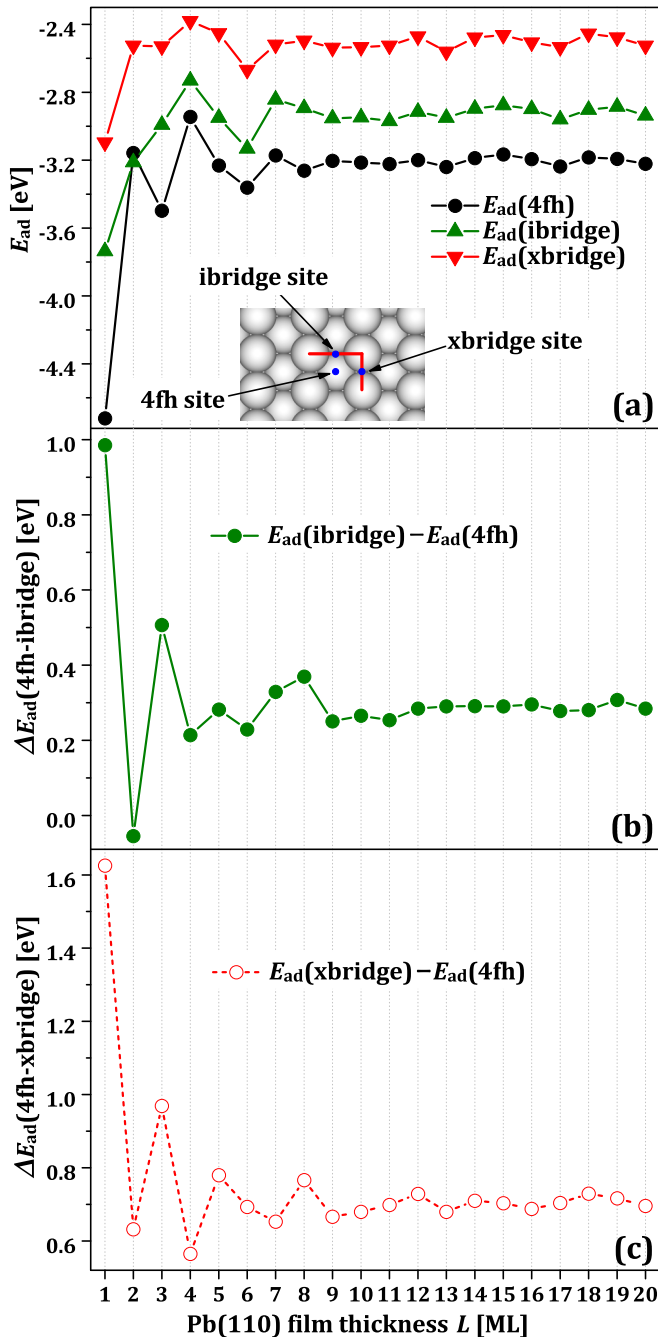


FIG. 9. (a) Adsorption energies $E_{ad}(4fh)$, $E_{ad}(ibridge)$, and $E_{ad}(xbridge)$ of Pb adatom at 4fh, in-channel bridge, and cross-channel bridge sites versus Pb(110) film thickness L from our PBEsol calculations, respectively. Inset illustrates the 4fh, in-channel bridge, and cross-channel bridge sites of Pb(110) surface. (b) Adsorption energy difference $\Delta E_{ad}(4fh-ibridge)$ between 4fh site and in-channel bridge site. (c) Adsorption energy difference $\Delta E_{ad}(4fh-xbridge)$ between 4fh site and cross-channel bridge site.

bridge sites, versus Pb(110) film thickness L are shown in Fig. 9(a). Compared with Figs. 1(e) and 1(f), the E_{ad} curves in Fig. 9(a) retain similar features to the corresponding γ or $\Delta\mu$ curve. In all DFT calculations for Fig. 9, we choose a 4×5 unit cell with the \mathbf{k} mesh of $9 \times 9 \times 1$, and fix the bottom 1 ML but allow to relax other atoms.

B. Diffusion barriers

To obtain the energy barrier of a Pb adatom hopping over an in-channel or cross-channel bridge, we first simply calculate the energy difference $\Delta E_{ad}(4fh-bridge) = E_{ad}(bridge) - E_{ad}(4fh)$, as expressed in Eq. (9). $\Delta E_{ad}(4fh-ibridge)$ and $\Delta E_{ad}(4fh-xbridge)$, where ibridge (xbridge) denotes in-channel (cross-channel) bridge, oscillate for $L < 6$ out-of-phase with $E_{ad}(4fh)$ in Fig. 9(a), but they become more irregular for $L > 6$, as shown in Figs. 9(b) and 9(c), respectively.

From Fig. 9(b), $\Delta E_{ad}(4fh-ibridge)$ at $L = 2$ is negative, i.e., the energy of the Pb adatom at the in-channel bridge is lower than that at the 4fh site. Thus, to obtain the diffusion barrier, we have to perform a cNEB calculation in this case. We find that the MEP between an adjacent 4fh and in-channel bridge sites is single-peaked, with a TS midway between these two sites. This TS is 71 (82) meV higher than the in-channel bridge site energy from our PBEsol (PBE) cNEB calculation. This difference corresponds to the hopping barrier. Except for this special case, all other $\Delta E_{ad}(4fh-ibridge)$ and $\Delta E_{ad}(4fh-xbridge)$ are always positive, as shown in Figs. 9(b) and 9(c), and correspond to adatom hopping barriers. To confirm this assignment, we also performed the PBEsol and PBE cNEB calculations for Pb adatom hopping over the in-channel and cross-channel bridges on a 5-ML Pb(110) film, and obtained a single-peaked MEP curve with the TS at the bridge site. From the above analysis, we conclude that the hopping barrier over the in-channel bridge is much smaller than that for the cross-channel bridge for any thickness. See Figs. 9(b) and 9(c). Additional results are reported in Table S9 [64].

Next, we characterize exchange diffusion. We first perform a PBEsol cNEB calculation for a two-atom in-channel exchange on a 5-ML Pb(110) film, and the obtained MEP is shown in Fig. 10. Unlike exchange on Pb(100) film (where the MEP is single-peaked) in Fig. 7, the MEP in Fig. 10 is double-peaked, and the symmetric configuration (see the image 06) is not a saddle point but a local minimum. Therefore, one cannot use a SR method to simply obtain the in-channel exchange barrier for a (110) surface. Obviously, two saddle points around images 04 and 08 are symmetric, and yield a barrier of 514 meV, which is larger than the

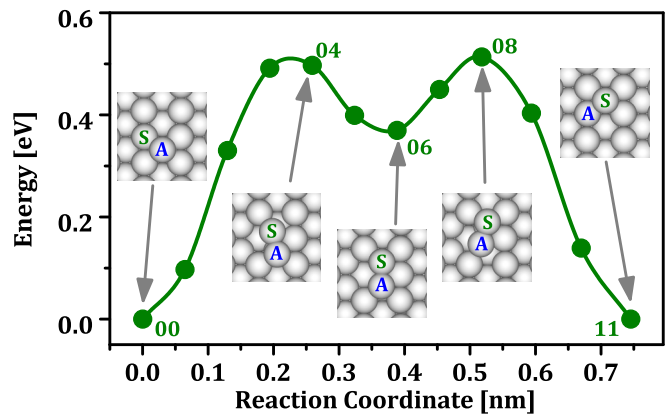


FIG. 10. The MEP of a two-atom in-channel exchange on a 5-ML Pb(110) film from our PBEsol cNEB calculation. Inset indicates the configurations of key images (00, 04, 06, 08, and 11) during the exchange of adatom A and surface atom S.

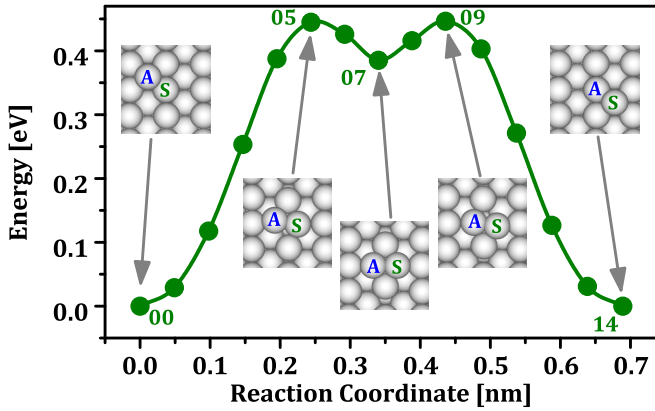


FIG. 11. The MEP of a two-atom cross-channel exchange on a 5-ML Pb(110) film from our PBEsol cNEB calculation. Inset indicates the configurations of key images (00, 05, 07, 09, and 14) during the exchange of adatom A and surface atom S.

hopping barrier over the in-channel bridge but significantly smaller than that over the cross-channel bridge (see Table S9 for hopping barriers [64]). We note that the MEP curve shape in Fig. 10 is similar to that for Al(110) surface [47], where the MEP is also double-peaked.

Second, we perform a PBEsol cNEB calculation for a two-atom cross-channel exchange on a 5-ML Pb(110) film, and obtain a double-peaked MEP with two TS around images 05 and 09, the corresponding barrier being 446 meV, as shown in Fig. 11. Note that the symmetric configuration (see the inset for image 07 in Fig. 11) is a local minimum of 61 meV below the two TS. This feature of MEP is different from that for the Al/Al(110) system, where the symmetric configuration corresponds to the TS instead of a local minimum [47]. Due to the geometric symmetry of image 07, there is an alternate two-atom in-channel exchange [47] with the same diffusion barrier (i.e., 446 meV) as that of the cross-channel exchange.

According to Fichthorn *et al.*'s accelerated *ab initio* MD simulations for Al/Al(110) [47,76], there is a dominant diagonal exchange pathway for diffusion in the cross-channel direction, for which no symmetric configuration is observed along the MEP. For Pb/Pb(110), we also obtain an analogous MEP when an initial cNEB trial path (denoted as path I), which is simply from a linear interpolation between two endpoints (images 00 and 14), is chosen. However, the associated single-peaked MEP yields a barrier of 474 meV, which is 28 meV higher than that for the cross-channel exchange pathway in Fig. 11. Thus, this diagonal exchange mechanism does not dominate that in Fig. 11. For the latter, we used an initial cNEB path (denoted as path II), which is a combination of two MEPs separately obtained from 00 to 07 and from 07 to 14, respectively. These results indicate that there are multiple MEPs for the cross-channel exchange, which can be obtained by taking different initial paths in the cNEB calculations.

For comparison, we also perform the cNEB calculations using PBE functional for cross-channel exchange. Taking path II as the initial path, we obtain a double-peaked MEP similar to the PBEsol result in Fig. 11, and the corresponding barrier is 416 meV. Taking path I as the initial path, we find that the MEP curve has a shape transformation from single- to double-peaked, finally optimized back to the shape obtained by taking

path II as the initial path. For the above PBEsol calculations, however, we do not find such a MEP shape transformation.

VI. DISCUSSION OF ISLAND FORMATION ON Pb(111)

As noted in Sec. I, there exist several studies of Pb island formation during Pb deposition on Pb(111) nanofilms of different thicknesses supported on Si(111)-(7 × 7) at $T = 40$ K with a deposition rate of around $F = 10^{-3}/s$ [19,21,24]. These studies have provided high-quality STM data for island densities and structures for both stable and unstable film thicknesses. The key feature is that the island density on a stable film is lower by a factor of 60 than on an unstable film. The islands on the stable film are correspondingly far larger with linear span from 40 to 60 nm and have a fully developed fractal shape with arms of approximate width 3 to 5 nm. In contrast, the smaller islands of diameter around 5 to 7 nm on the unstable film are irregular but more compact shapes. Let $E_{d,s}$ ($E_{d,u}$) denote the diffusion barrier on the stable (unstable) film. For irreversible island formation on both films, the difference in density $\propto e^{E_d/(3k_B T)}$ would correspond to $E_{d,u} - E_{d,s} \approx 40$ meV. This variation is somewhat larger than the maximum variation around 30 meV in our DFT results E_d for *unsupported* films in the range $L = 3$ to 12 [see Fig. 3(c)]. Thus, one might question this interpretation, although it perhaps cannot be ruled out.

With regard to the assumption of irreversible island formation, this requires that the crossover parameter

$$Y = \frac{\nu}{F} e^{-(E_d + 1.5\omega_{p1}^*)/(k_B T)} \quad (11)$$

is below about $Y_c \approx 10$, where ω_{p1}^* is a suitably defined NN pair interaction, and again ν denotes the attempt frequency for hopping [77]. This formulation is based on a model with NN interactions ω_{p1}^* , and where trimers are significantly more stable than dimers, as is satisfied for Pb/Pb(111). The appropriate designation for the NN pair interaction for Pb/Pb(111) is $\omega_{p1}^* = \omega_{p1}(\text{fcc}) - 2\Delta E_{ad}(\text{hcp-fcc})$, accounting for the weaker adsorption energy of fcc sites (preferred by the dimer) relative to hcp sites (preferred by adatoms). Given the large value of $\omega_{p1}^* \approx 0.5$ eV, one finds that Y is far below Y_c for any reasonable choice of the other parameters (e.g., E_d anywhere in the range of 0.02 to 0.05 eV), indicating that island formation should be irreversible. In contrast, previous modeling [24] used a large $E_d = 0.063$ eV and small $\omega_{p1}^* = 0.017$ eV, together with the choice of prefactor $\nu \approx 10^{11}/s$, which corresponds to reversible island formation. However, this modeling enforced a critical size $i = 1$ for islands on unstable films generating a high island density. Another issue is whether the observed fractal islands can be achieved for large critical size (where atoms can readily detach from kink sites which facilitates formation of compact islands), as suggested in previous work. However, we do not pursue this issue here.

For Pb(111), as described in Sec. III B, the hopping barrier is very low, comparable to the thermal energy at room temperature. In this regime, the Arrhenius expression Eq. (6) may not reliably describe diffusion due to barrier recrossing and other features. However, this approach is still reliable for the low- T regime which is often of experimental interest for fcc (111) surface. However, for higher barriers occurring in

other cases, the Arrhenius form is reliable, and can, e.g., give an accurate assessment of the relative contributions of hopping and exchange to diffusion.

VII. SUMMARY

We have performed the first-principles DFT calculations using PBEsol and PBE functionals to investigate key energetics of Pb adatoms on Pb(111), Pb(100), and Pb(110) nanofilms of various thicknesses. Both adsorption energy and diffusion barrier as a function of film thickness exhibit a damped oscillatory form. The presence of adatoms adsorbed on the nanofilm surface will perturb the regularity of oscillations seen in the thickness-dependent properties (e.g., surface energies) of perfect slabs. The perturbation is strong for both Pb(111) and Pb(110) nanofilms, and relatively weak for Pb(100).

For a Pb(111) nanofilm, our cNEB calculations often reveal a double-peaked MEP form for Pb adatom hopping between adjacent fcc and hcp sites. This behavior is different from the typically expected and previously reported single-peaked MEPs for other metal-on-metal(111) systems. For bulk Pb(111) film, we obtain an estimated PBEsol (PBE) hopping barrier of 28 (39) meV, much lower than that for three types of two-atom exchange diffusion barriers of 300 meV or above.

For a Pb(100) film, the estimated PBEsol (PBE) hopping barrier is 725 (678) meV, which is much higher than the two-atom diagonal exchange diffusion barrier of 273 (252) meV along the $\langle 100 \rangle$ direction. We also obtain a PBEsol two-atom exchange barrier of 559 meV (which is in between the hopping and diagonal diffusion barriers) along the $\langle 110 \rangle$ direction.

For a Pb(110) film, the estimates from our PBEsol (PBE) calculations for the hopping barrier over in-channel and cross-channel bridges are 289 (247) and 707 (599) meV, respectively. We also obtain a PBEsol two-atom in-channel exchange barrier of 514 meV, and a PBEsol (PBE) two-atom cross-channel exchange barrier of 446 (416) meV. We find that the MEP for the two-atom cross-channel exchange on Pb(110) is double-peaked, and therefore different from the single-peaked MEP obtained from previous calculations for Al/Al(110) system [47].

The diffusion barrier values obtained from our DFT calculations for Pb(111) and Pb(100) have significant differences from very limited results in previous literature (including those from the early empirical MEAM potential [67] and recent DFT calculations [30]). The diffusion barriers for Pb(110) were not available before our work. We believe that the energetic parameters and diffusion paths obtained from this work will be crucial to understand and reliably simulate the epitaxial growth of Pb nanostructures.

Finally, we mention one caveat with the above analysis. Given that Pb is a heavy element, one might consider the possibility that spin-orbit coupling (SOC) could modify some electronic properties. However, this issue has not been considered in any of the multiple previously published DFT analyses of adsorption and diffusion processes in Pb surface systems. Thus, we have performed several calculations of SOC effects on various energies.

For bulk properties, SOC has little effect on lattice constant, but does significantly impact cohesion energy (although the latter does not necessarily translate to a significant effect on

surface properties of most interest). For the surface energies of key interest, analysis incorporating SOC produces the same trends for all three surfaces up to 7 ML (matching the strong oscillations and other variations) shown in Fig. 1 for analysis without SOC. We now include these results in Fig. S2 of the Supplemental Material [64]. Our additional preliminary analysis does suggest some deviations in trends for larger thicknesses, mainly for the (111) surface. Also, the limiting value for surface energy for bulk films is modified by SOC (as is clear by comparing Fig. 1 with Fig. S2), but this does not affect the thickness-dependent relative film stability, which is of particular experimental interest. We have performed initial analysis (incorporating some approximations to aid computational efficiency) on other quantities including diffusion barriers. SOC has some effects on the barriers for Pb(111) for $L = 1$ to 3, but little effect for $L = 4$ to 7 (preserving bilayer oscillations). For hopping and exchange on Pb(100) and Pb(110), preliminary approximate analysis reveals that SOC effects do not change the form of the variation of barrier with film thickness, but produces somewhat lower barriers by roughly 10% to 20%.

ACKNOWLEDGMENTS

W.L. and L.H. acknowledge support from startup funds from Southern University of Science and Technology and from NSFC under Grant No. 11404160. J.W.E. and Y.H. were supported for this work by NSF Grant No. CHE-1507223, and their work was performed at Ames Laboratory which is operated for the U. S. Department of Energy (USDOE) by Iowa State University under Contract No. DE-AC02-07CH11358. Y.H. thanks G. Henkelman for his helpful communication regarding the cNEB calculation for cross-channel exchange on Pb(110). Our computations utilized the resources from the NSF-supported Extreme Science and Engineering Discovery Environment (XSEDE) served by Texas Advanced Computing Center (TACC), the USDOE-supported National Energy Research Scientific Computing Center (NERSC), and the Center for High Performance Computing (CHPC) at University of Utah.

APPENDIX A: INTERLAYER RELAXATION EFFECTS ON SURFACE ENERGIES

For Pb(111) thin films with thickness $L > 1$, due to the interlayer relaxation, the interlayer spacing will vary within the film about an average value \bar{d} , which also deviates from the bulk value. Also, the Fermi wavelength, denoted by $\tilde{\lambda}_F$, which depends on \bar{d} , will also correspondingly deviate. Consequently, the “beat period” $\tilde{\Lambda}$ will not exactly equal the previously cited $\Lambda = 7.42$ for different L because $\bar{d}/\tilde{\lambda}_F$ is not generally equal to d/λ_F [see Eq. (4)]. Figure 12(a) shows the variation in the interlayer relaxation (characterized by \bar{d}) as a function of L . For all $L > 1$, $\bar{d} - d < 0$, i.e., the films shrink relative to the bulk. Larger $|\bar{d} - d|$ results in larger $|\tilde{\Lambda} - \Lambda|$, as shown in Fig. 12(b). Around a switch point, the shape of γ or $\Delta\mu$ curve is particularly sensitive to the value of $\tilde{\Lambda}$. Specifically, for $L = 7$, $\tilde{\Lambda}$ becomes 5.91 after relaxation from $\Lambda = 7.42$ before relaxation, and thus the first beat period of γ or $\Delta\mu$ curve is shortened by ~ 1 ML, as mentioned in Sec. II B.

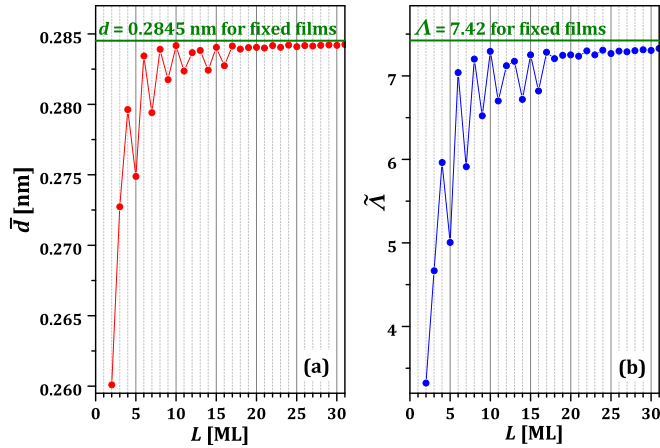


FIG. 12. (a) Average interlayer spacing \bar{d} , and (b) beat period $\bar{\Lambda}$ versus relaxed Pb(111) film thickness L from our PBEsol calculations. Horizontal green lines indicate the constant values of \bar{d} and $\bar{\Lambda}$ for the films fixed to bulk lattice.

Comparing relaxation effects for Pb(100) and Pb(110), those for Pb(110) are larger overall, and the damping of the average interlayer spacing \bar{d} (not shown here) with increasing L is slower.

APPENDIX B: ADATOM-INDUCED INTRALAYER RELAXATION

After an adatom is adsorbed on a surface, *intralayer* relaxation occurs especially for the top ML around the adsorption site on substrate. In Sec. II B and Appendix A we have discussed the effects of interlayer relaxation on the curves of γ and $\Delta\mu$ versus L . In contrast to the black curves in Figs. 1(a) and 1(b), the adsorption curves in Fig. 3(a) become much more irregular than the red curves in Figs. 1(a) and 1(b). This indicates that the intralayer relaxation induced by the adatom produces much stronger disruption upon the regularity of oscillations in E_{ad} (than that seen for γ and $\Delta\mu$ versus L) due to interlayer relaxation of the clean substrate.

In calculations of Fig. 3, we use a 5×5 unit cell, which corresponds an adatom coverage of 0.04 ML. It appears that even for such small finite coverages, the adsorbed adatoms can strongly alter the shape of quantum well and the uniformity of electron distribution in a film versus a uniform jellium slab [33] without the adatoms and therefore leads to significant changes in quantum well states (QWSs) and corresponding eigenvalues, which depend on the perturbation details. Schwingenschlöl *et al.* performed DFT calculations for the influence of Co adatoms on the QWSs existing in Cu/Co(100) multilayers, and found that the typical oscillations of the density of states at the Fermi level as a function of Cu(100) film thickness are strongly perturbed by the presence of adatoms on the surface [78].

In addition, making a comparison from Fig. 3(a) (for a monomer) to Fig. 4(a) (for a dimer) to Fig. 4(c) (for a trimer) to Fig. 4(e) (for a 1 ML) within a 5×5 unit cell, we also note the evolution of the adsorption energy variation with L from irregular to regular with increasing adatom coverage by increasing the adsorbate size. Specifically, there is a switch in

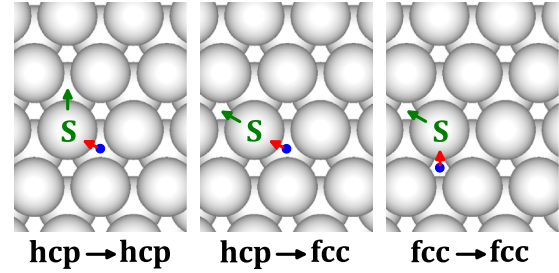


FIG. 13. Schematics for three types of exchange between an initial adatom (blue dot) and one surface atom (labeled as S) of (111) surface. A red arrow indicates that the initial adatom kicks the surface atom S out of the surface lattice and takes the place of the atom S; a green arrow indicates that the atom S is pushed to an adjacent hcp or fcc site and becomes a new adatom.

energy magnitude at $L = 4$ and 5 from E_{ad} to E_{p1} to E_{t1} , and finally to E_{1ML} .

APPENDIX C: TWO-ATOM EXCHANGE ON Pb(111)

A fcc (111) surface has the most close-packed geometry relative to other indexed planes, and therefore it is expected that the exchange diffusion between the adatom and one atom of the (111) surface should be the least unfavorable relative to adatom hopping [79]. Nevertheless, here we want to confirm this expectation by calculating the exchange diffusion barriers of Pb adatom on Pb(111). As shown in Fig. 13, there are three types of exchange between the adatom and one of its adjacent surface atoms on a (111) surface: (i) hcp \rightarrow hcp, where the adatom is initially at a hcp site, and the surface atom is pushed to another NN hcp site; (ii) hcp \rightarrow fcc (fcc \rightarrow hcp), where the adatom is initially at a hcp (fcc) site, and the surface atom is pushed to a NN fcc (hcp) site; and (iii) fcc \rightarrow fcc, where the adatom is initially at a fcc site, and the surface atom is pushed to another NN fcc site. hcp \rightarrow fcc and fcc \rightarrow hcp are reverse processes of each other and thus share the same MEP.

In Table III we list the diffusion barriers for three types of two-atom exchange mechanism from our PBEsol and PBE calculations for Pb adatom on a 5-ML Pb(111) film. From Table III the type of hcp \rightarrow hcp has the smallest exchange

TABLE III. Diffusion barriers E_d for three types (hcp \rightarrow hcp, hcp \rightarrow fcc, and fcc \rightarrow fcc) of two-atom exchange mechanism from our PBEsol and PBE calculations for Pb adatom on a 5-ML Pb(111) film using 3×3 and 5×5 unit cells. All energies are in units of meV. In these cNEB calculations for exchange, we always use 15 images plus 2 endpoints.

	PBEsol	PBE	PBE
Unit cell size	5×5	5×5	3×3^a
\mathbf{k} mesh	$9 \times 9 \times 1$	$9 \times 9 \times 1$	$11 \times 11 \times 1$
hcp \rightarrow hcp	380	300	366
hcp \rightarrow fcc	402	333	383
fcc \rightarrow fcc	479	394	358

^aUsing a 3×3 unit cell with a \mathbf{k} mesh of $5 \times 5 \times 1$ and optimizing uppermost 2 ML of 5-ML Pb(111) substrate, Lin *et al.* obtain a PBE exchange barrier of 110 meV [30].

barrier of 380 (300) meV from our PBEsol (PBE) calculation with a 5×5 unit cell. This value is much larger than the corresponding hopping barrier of 20 (27) meV in Table S2 [64]. Because Lin *et al.* obtained a PBE exchange barrier of only 110 meV using a 3×3 unit cell [30], we also use the same unit cell size, but obtain a PBE exchange barrier of 358 meV at least (see Table III). Thus, our results for two-atom exchange barrier of Pb on Pb(111) are significantly different from Lin *et al.*'s result.

Finally, we mention that most of our obtained MEP curves (not shown) from the cNEB method for the above three types of two-atom exchange mechanism are double-peaked, but we find that the curve shape sometimes sensitively depends on the initial geometry or unit cell size, e.g., for the type of fcc \rightarrow fcc exchange, we obtain a single-peaked MEP curve when using a 5×5 unit cell, while it is double-peaked when using a 3×3 unit cell.

APPENDIX D: TWO-ATOM EXCHANGE ON Pb(100)

Here we also provide the details for how to appropriately build the initial symmetric geometry when one uses the SR method to obtain the two-atom exchange diffusion barrier. Obviously there are many choices of two-atom separation and the atom height for the initial geometry, but a judicious choice can make the energy optimization efficient. In Fig. 14 we

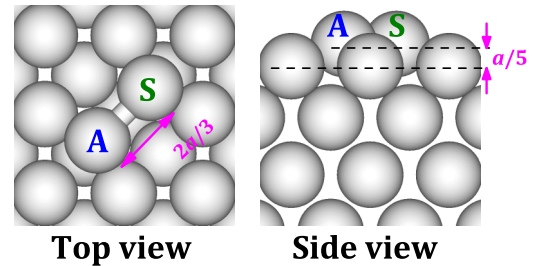


FIG. 14. Schematic of initial geometry used to directly obtain the TS or saddle point for two-atom diagonal exchange diffusion on a fcc or bcc (100) surface by the SR method. After full relaxation, it is optimized to the geometry indicated in the middle image of the inset of Fig. 6(c).

illustrate an experiential initial geometry that the adatom A and the surface atom S are separated by $2a/3$ along the diagonal and symmetrically aligned above the vacancy left by S; the height of both A and S is set to be $a/5$. After full relaxation, the initial geometry in Fig. 14 will be optimized to the TS (or saddle-point) configuration which is indicated in the middle image of the inset of Fig. 6(c). The geometry in Fig. 14 as an initial configuration is actually already used in our previous work to efficiently calculate the exchange barriers for other metal-on-metal(100) systems [74].

-
- [1] W. B. Su, S. H. Chang, W. B. Jian, C. S. Chang, L. J. Chen, and T. T. Tsong, *Phys. Rev. Lett.* **86**, 5116 (2001).
- [2] H. Okamoto, D. Chen, and T. Yamada, *Phys. Rev. Lett.* **89**, 256101 (2002).
- [3] R. Otero, A. L. V. de Parga, and R. Miranda, *Phys. Rev. B* **66**, 115401 (2002).
- [4] H. P. Bonzel, *Phys. Rep.* **385**, 1 (2003).
- [5] A. Menzel, M. Kammler, E. H. Conrad, V. Yeh, M. Hupalo, and M. C. Tringides, *Phys. Rev. B* **67**, 165314 (2003).
- [6] H. Hong, C.-M. Wei, M. Y. Chou, Z. Wu, L. Basile, H. Chen, M. Holt, and T.-C. Chiang, *Phys. Rev. Lett.* **90**, 076104 (2003).
- [7] C.-S. Jiang, S.-C. Li, H.-B. Yu, D. Eom, X.-D. Wang, P. Ebert, J.-F. Jia, Q.-K. Xue, and C.-K. Shih, *Phys. Rev. Lett.* **92**, 106104 (2004).
- [8] Y. Han, J. Y. Zhu, F. Liu, S.-C. Li, J.-F. Jia, Y.-F. Zhang, and Q.-K. Xue, *Phys. Rev. Lett.* **93**, 106102 (2004).
- [9] M. H. Upton, C. M. Wei, M. Y. Chou, T. Miller, and T.-C. Chiang, *Phys. Rev. Lett.* **93**, 026802 (2004).
- [10] P. Czochke, H. Hong, L. Basile, and T.-C. Chiang, *Phys. Rev. Lett.* **93**, 036103 (2004).
- [11] Y.-F. Zhang, J.-F. Jia, T.-Z. Han, Z. Tang, Q.-T. Shen, Y. Guo, Z. Q. Qiu, and Q.-K. Xue, *Phys. Rev. Lett.* **95**, 096802 (2005).
- [12] M. M. Özer, Y. Jia, B. Wu, Z. Zhang, and H. H. Weiering, *Phys. Rev. B* **72**, 113409 (2005).
- [13] T.-L. Chan, C. Z. Wang, M. Hupalo, M. C. Tringides, and K. M. Ho, *Phys. Rev. Lett.* **96**, 226102 (2006).
- [14] S.-C. Li, J.-F. Jia, X. Ma, Q.-K. Xue, Y. Han, and F. Liu, *Appl. Phys. Lett.* **89**, 123111 (2006).
- [15] Z. Kuntova, M. Hupalo, Z. Chvoj, and M. Tringides, *Surf. Sci.* **600**, 4765 (2006).
- [16] M. Hupalo and M. C. Tringides, *Phys. Rev. B* **75**, 235443 (2007).
- [17] Z. Kuntova, M. Hupalo, Z. Chvoj, and M. C. Tringides, *Phys. Rev. B* **75**, 205436 (2007).
- [18] Z. Kuntová, M. C. Tringides, and Z. Chvoj, *Phys. Rev. B* **78**, 155431 (2008).
- [19] S. M. Binz, M. Hupalo, and M. C. Tringides, *Phys. Rev. B* **78**, 193407 (2008).
- [20] Y. Han, F. Liu, S.-C. Li, J.-F. Jia, Q.-K. Xue, and B.-J. Lee, *Appl. Phys. Lett.* **92**, 021909 (2008).
- [21] S. M. Binz, M. Hupalo, and M. C. Tringides, *J. Appl. Phys.* **105**, 094307 (2009).
- [22] M. Li, C. Z. Wang, J. W. Evans, M. Hupalo, M. C. Tringides, and K. M. Ho, *Phys. Rev. B* **79**, 113404 (2009).
- [23] Y. Han, B. Ůnal, D. Jing, P. A. Thiel, J. W. Evans, and D.-J. Liu, *Materials* **3**, 3965 (2010).
- [24] Z. Kuntová, M. C. Tringides, S. M. Binz, M. Hupalo, and Z. Chvoj, *Surf. Sci.* **604**, 519 (2010).
- [25] J. Kim, S. Qin, W. Yao, Q. Niu, M. Y. Chou, and C.-K. Shih, *Proc. Natl. Acad. Sci. USA* **107**, 12761 (2010).
- [26] S.-J. Tang, C.-Y. Lee, C.-C. Huang, T.-R. Chang, C.-M. Cheng, K.-D. Tsuei, H.-T. Jeng, V. Yeh, and T.-C. Chiang, *Phys. Rev. Lett.* **107**, 066802 (2011).
- [27] L. Huang, C. Z. Wang, M. Z. Li, and K. M. Ho, *Phys. Rev. Lett.* **108**, 026101 (2012).
- [28] J. Kim, C. Zhang, J. Kim, H. Gao, M.-Y. Chou, and C.-K. Shih, *Phys. Rev. B* **87**, 245432 (2013).
- [29] K. Miśków, A. Krupski, and K. Wandelt, *Vacuum* **101**, 71 (2014).
- [30] X. Lin, A. Dasgupta, F. Xie, T. Schimmel, F. Evers, and A. Groß, *Electrochim. Acta* **140**, 505 (2014).

- [31] M. Jałochowski, R. Zdyb, and M. C. Tringides, *Phys. Rev. Lett.* **116**, 086101 (2016).
- [32] M. Müller, C. Salgado, N. Néel, J. J. Palacios, and J. Kröger, *Phys. Rev. B* **93**, 235402 (2016).
- [33] F. K. Schulte, *Surf. Sci.* **55**, 427 (1976).
- [34] B. J. Hinch, C. Koziol, J. P. Toennies, and G. Zhang, *Europhys. Lett.* **10**, 341 (1989).
- [35] T. Miller, M. Y. Chou, and T.-C. Chiang, *Phys. Rev. Lett.* **102**, 236803 (2009).
- [36] Y. Han and D.-J. Liu, *Phys. Rev. B* **80**, 155404 (2009).
- [37] R.-Y. Liu, A. Huang, C.-C. Huang, C.-Y. Lee, C.-H. Lin, C.-M. Cheng, K.-D. Tsuei, H.-T. Jeng, I. Matsuda, and S.-J. Tang, *Phys. Rev. B* **92**, 115415 (2015).
- [38] Y. Guo, Y.-F. Zhang, X.-Y. Bao, T.-Z. Han, Z. Tang, L.-X. Zhang, W.-G. Zhu, E. G. Wang, Q. Niu, Z. Q. Qiu, J.-F. Jia, Z.-X. Zhao, and Q.-K. Xue, *Science* **306**, 1915 (2004).
- [39] X.-Y. Bao, Y.-F. Zhang, Y. Wang, J.-F. Jia, Q.-K. Xue, X. C. Xie, and Z.-X. Zhao, *Phys. Rev. Lett.* **95**, 247005 (2005).
- [40] T.-Z. Han, G.-C. Dong, Q.-T. Shen, Y.-F. Zhang, J.-F. Jia, and Q.-K. Xue, *Appl. Phys. Lett.* **89**, 183109 (2006).
- [41] Y.-F. Zhang, Z. Tang, T.-Z. Han, X.-C. Ma, J.-F. Jia, Q.-K. Xue, K. Xun, and S.-C. Wu, *Appl. Phys. Lett.* **90**, 093120 (2007).
- [42] F.-Q. Xie, L. Nittler, C. Obermair, and T. Schimmel, *Phys. Rev. Lett.* **93**, 128303 (2004).
- [43] F.-Q. Xie, F. Hüser, F. Pauly, C. Obermair, G. Schön, and T. Schimmel, *Phys. Rev. B* **82**, 075417 (2010).
- [44] G. Henkelman, B. P. Uberuaga, and H. Jónsson, *J. Chem. Phys.* **113**, 9901 (2000).
- [45] G. Henkelman and H. Jónsson, *J. Chem. Phys.* **113**, 9978 (2000).
- [46] P. J. Feibelman, *Phys. Rev. Lett.* **65**, 729 (1990).
- [47] Y. Tiwary and K. A. Fichthorn, *Phys. Rev. B* **81**, 195421 (2010).
- [48] G. Kresse and J. Hafner, *Phys. Rev. B* **47**, 558 (1993).
- [49] G. Kresse and J. Furthmüller, *Phys. Rev. B* **54**, 11169 (1996).
- [50] G. Kresse and D. Joubert, *Phys. Rev. B* **59**, 1758 (1999).
- [51] C. M. Wei and M. Y. Chou, *Phys. Rev. B* **66**, 233408 (2002).
- [52] C. M. Wei and M. Y. Chou, *Phys. Rev. B* **75**, 195417 (2007).
- [53] D. Vanderbilt, *Phys. Rev. B* **41**, 7892 (1990).
- [54] P. E. Blöchl, *Phys. Rev. B* **50**, 17953 (1994).
- [55] J. P. Perdew, A. Ruzsinszky, G. I. Csonka, O. A. Vydrov, G. E. Scuseria, L. A. Constantin, X. Zhou, and K. Burke, *Phys. Rev. Lett.* **100**, 136406 (2008).
- [56] W. Joss, *Phys. Rev. B* **23**, 4913 (1981).
- [57] C. Kittel, *Introduction to Solid State Physics*, 7th ed. (John Wiley & Sons, New York, 1996).
- [58] R. Gaudoin and W. M. C. Foulkes, *Phys. Rev. B* **66**, 052104 (2002).
- [59] R. Feder and A. S. Nowick, *Phys. Rev.* **109**, 1959 (1958).
- [60] B. T. A. McKee, W. Triftshäuser, and A. T. Stewart, *Phys. Rev. Lett.* **28**, 358 (1972).
- [61] Y. Hara and S. Nanao, *Point Defects and Defect Interactions in Metals*, edited by J. Takamura *et al.* (North-Holland, Amsterdam, 1982).
- [62] D. Yu, M. Scheffler, and M. Persson, *Phys. Rev. B* **74**, 113401 (2006).
- [63] Y. Han, J. W. Evans, and D.-J. Liu, *Surf. Sci.* **602**, 2532 (2008).
- [64] See Supplemental Material at <http://link.aps.org/supplemental/10.1103/PhysRevB.96.205409> for (i) how to extract convergent surface energies from slab calculations, (ii) analysis of the effects of spin-orbit coupling for Pb systems on surface properties, and (iii) data for energetics of Pb adatoms on Pb(111), Pb(100), and Pb(110) nanolm surfaces from our DFT first-principles calculations.
- [65] C. Bombis, A. Emundts, M. Nowicki, and H. P. Bonzel, *Surf. Sci.* **511**, 83 (2002).
- [66] G. Farin, *Curves and Surfaces for CAGD: A Practical Guide*, 5th ed. (Academic, San Diego, 2002).
- [67] Y. Han, G.-H. Lu, B.-J. Lee, and F. Liu, *Surf. Sci.* **602**, 2284 (2008).
- [68] A. Bogicevic, S. Oveson, P. Hyldgaard, B. I. Lundqvist, H. Brune, and D. R. Jennison, *Phys. Rev. Lett.* **85**, 1910 (2000).
- [69] S. S. Hayat, M. A. Ortigoza, M. A. Choudhry, and T. S. Rahman, *Phys. Rev. B* **82**, 085405 (2010).
- [70] L.-Y. Ma, L. Tang, Z.-L. Guan, K. He, K. An, X.-C. Ma, J.-F. Jia, Q.-K. Xue, Y. Han, S. Huang, and F. Liu, *Phys. Rev. Lett.* **97**, 266102 (2006).
- [71] M. Karimi, T. Tomkowski, G. Vidali, and O. Biham, *Phys. Rev. B* **52**, 5364 (1995).
- [72] R. Stumpf and M. Scheffler, *Phys. Rev. B* **53**, 4958 (1996).
- [73] C. M. Chang and C. M. Wei, *Chin. J. Phys.* **43**, 169 (2005).
- [74] Y. Han, C. R. Stoldt, P. A. Thiel, and J. W. Evans, *J. Phys. Chem. C* **120**, 21617 (2016).
- [75] C. M. Chang, C. M. Wei, and J. Hafner, *J. Phys.: Condens. Matter* **13**, L321 (2001).
- [76] K. A. Fichthorn, R. A. Miron, Y. Wang, and Y. Tiwary, *J. Phys.: Condens. Matter* **21**, 084212 (2009).
- [77] J. W. Evans, P. A. Thiel, and M. C. Bartelt, *Surf. Sci. Rep.* **61**, 1 (2006).
- [78] U. Schwingenschlögl, T. Uchihashi, C. D. Paola, and R. Berndt, *Phys. Rev. B* **82**, 033406 (2010).
- [79] H. Bulou and C. Massobrio, *Phys. Rev. B* **72**, 205427 (2005).